24 Image Fusion in Remote Sensing with the Steered Hermite Transform

Boris Escalante-Ramírez and Alejandra A. López-Caloca

CONTENTS

24.1 Introduction 485
24.2 The Hermite Transform 487
24.2.1 The Hermite Transform as an Image Representation Model 487
24.2.2 The Steered Hermite Transform 489
24.3 Fusion Method Based on the Hermite Transform 491
24.3.1 Fusion Scheme with Multispectral and Panchromatic Images 491
24.3.2 Fusion Scheme with Multispectral Images and SAR Image 493
24.3.3 Noise Reduction with the Hermite Transform 493
24.3.4 Image Fusion 494
24.4 Experimental Results 495
24.4.1 Multispectral and Panchromatic Image Fusion 495
24.4.1.1 Visual Quality 496
24.4.1.2 Spectral Quality and Spatial Quality 497
24.4.1.3 Red Versus NIR Dispersion Diagrams 498
24.4.2 Multispectral and SAR Image Fusion 498
24.4.2.1 Visual Quality 500
24.4.2.2 Spectral Quality 500
24.4.2.3 Classification 500
24.5 Conclusions 500
Acknowledgments 502
References 502

24.1 INTRODUCTION

Advances in sensor technology have produced a large variety of sensors capable of capturing different kinds of information from the Earth's observation satellites, with different characteristics and modalities, depending on their use, for example, multisensor, multitemporary, multiresolution, and multifrequency [1–3]. Sensors, however, present technological limitations that affect image acquisition characteristics, for instance, multispectral (MS) sensors may capture images with high spectral resolution, but with lower spatial resolutions than panchromatic (PAN) sensor. Climate conditions also pose limitations to sensor technology as is the case of cloudy conditions that limit the range of optical sensors. Radar sensors overcome this limitation, but they are seriously impaired by the presence of speckle. Owing to these facts, in recent years, image fusion has become one of the most important and useful tasks for the remote sensing community.

The goal of image fusion is to integrate information from multiple sources, in order to create new images containing more information. The process of image fusion should not introduce any artifact

or inconsistency which may alter subsequent processes. It should be robust and tolerant to noise. As a result of a fusion process, two main characteristics are desirable: higher spatial resolution that can account for an adequate description of the shapes, features, and structures, and consistent spectral properties that allow the user to identify the different interacting objects.

There is a large variety of techniques described in the literature that tackle the problem of image fusion by incorporating high spatial resolution characteristics and keeping spectral properties from the same sensor. These approaches have evolved from simple linear combinations (intensity–hue–saturation) (IHS) [4,5] to methods based on principal component analysis (PCA) [6]. The main idea of fusion algorithms is to add spatial information to an image that is rich in spectral information, without modifying the latter. Methods like IHS and PCA improve the spatial quality, but they show spectral information distortion [7].

Recently, wavelet transform (WT)-based methods, with different approaches, have been widely used for image fusion. The discrete wavelet transform, either decimated [8–10] or nondecimated [11,12], has become very popular, multiresolution analysis being one of their most important properties. Decimated methods, implemented with dyadic structures based on the Mallat algorithm [13], present interesting properties, such as nonsymmetry and nonredundant descriptions. Their main disadvantage is the lack of shift invariance, meaning that small shifts of the input image produces very different wavelet coefficient contents. This limitation usually translates into artifacts introduced in the fused image. Shift invariance can be achieved with nondecimated methods, such as the "à trous" algorithm [14,15]. These methods imply redundant image descriptions that avoid decimation by inserting zeroes between the filter coefficients. Although they show better spatial reconstruction in comparison with decimated structures [7,16], they lose orientation selectivity. In this case, image decomposition consists of an approximated band and a single-detail image at each resolution level, resembling Laplacian or difference of Gaussian hierarchical structures. Among these methods, the additive wavelet method (AWL) developed by Nuñez et al. [12] has become a reference method. Later, González-Audícana et al. [17] found a way to incorporate the sensor's spectral properties to overcome the spectral distortion problem of traditional IHS fusion method, and developed the extended fast IHS method (eFIHS). They proved that this method performs as good as high computational cost methods based on nondecimated wavelet transforms.

Recently, the curvelet transform has been proposed as a tool for image fusion [18]. It consists of a multiresolution directional-oriented representation obtained from a nondecimated wavelet transform. Its results show the advantage of detecting and reconstructing oriented image patterns in image fusion products.

This chapter introduces the steered Hermite transform (HT) as an efficient representation model for image fusion.

Shift invariance and isotropic property (rotation) of the HT assures that no artifacts are introduced during the fusion process. The HT is also a good representation model for characteristic patterns such as edges, and lines, which may be extracted from the high-resolution PAN image and injected into the multispectral images, which results in images with a richer spatial content than the images obtained with processes like PCA and WT.

In particular, the rotation property of the HT [19,20] is relevant in the fusion process as it not only allows the detection of edges, but it also allows the estimation of other parameters, such as local orientation. Therefore, during the fusion process, patterns may be discriminated and selected according to their local energy and orientation. The use of the locally rotated HT provides a coefficient set with high-energy compaction, in such a way that few coefficients are needed to represent the more relevant image patterns needed for the fusion process.

One of the advantages of the HT over the WT is the use of a free subsampling parameter limited only by the support of the analysis window, that is, the only constraint for this parameter is that local analysis windows overlap with each other. This allows for the existence of decimated (subsampled) as well as the undecimated (no subsampling) HT decompositions. Both schemes are efficient for image fusion. Decimated structures are more efficiently computed, while undecimated structures

provide shift invariance to the decomposition, a highly valuable property that produces no artifacts in image reconstruction problems. In this chapter, two fusion applications with the HT are shown, single sensor (MS-PAN) and multisensor (MS-SAR). In the case of MS and SAR image fusion, adaptive speckle reduction in SAR images can be readily achieved within the HT analysis–synthesis process of the fusion scheme. For the first case, we compare our results with the eFIHS [17] and AWL methods [12] and for the second one, with the multisensor image fusion algorithms based on the generalized intensity modulation proposed in Ref. [21]. This scheme combines three kinds of images (MS-PAN-SAR) with speckle reduction achieved previously to the fusion process. In contrast, we show a fusion scheme where both speckle reduction and fusion can be achieved together.

The layout of this chapter is as follows. Section 24.2 introduces the Hermite transform. Section 24.3 presents two fusion methodologies; in the first, we fuse multispectral and panchromatic images from the same satellite with different spatial resolutions and in the second, we fuse different sensor images, namely, multispectral and SAR. Section 24.4 presents experiments conducted on SPOT-5, SAR AeS-1, and Landsat 7 + ETM images, with their respective fusion results. We show how the proposed method can help improve spatial resolution and keep spectral properties of the original MS images. Quality assessing of the synthesized images was determined by spectral quality fusion [10], spatial quality [9], scatterplot red–NIR [22], SAM [21], and in the case of SAR-MS fusion, classification of the fused product was also used for evaluation purposes. Finally, Section 24.5 presents the conclusions of this chapter.

24.2 THE HERMITE TRANSFORM

24.2.1 The Hermite Transform as an Image Representation Model

With the development of the scale-space theory in the 1980s, it has become evident that an efficient description of the elements that conforms an image is obtained through a multiresolution decomposition. The scale-space theory proves that the Gaussian function is optimal for this task. [23]. Most wavelet functions show irregular profiles, which makes them unsuitable for the representation of spatial phenomena in accordance to scale-space theory [24,25]. Among the computational representation models, which include important properties of human vision, we find the Gabor transform useful [26–29]. More recently, however, several authors have proven the limitations of this model from both neurophysiological and mathematical points of view. Q1

Stork and Wilson [30] reviewed neurophysiological measurements of others and analyzed psychophysical masking data and found that in many cases receptive-field functions other than Gabor functions fit better. They concluded that there are insufficient theoretical demonstrations and experimental data to favor Gabor functions over any of a number of other plausible receptive-field functions.

In contrast, Gaussian derivatives have been alternatively recognized as good models of the receptive field profiles of the human visual system [25,31–37]

Young made a comparison between both models and showed that the Gaussian model fits more accurately to the measurements of the signals at receptive fields of the human visual system, with the additional advantage of being orthogonal at the location of analysis [31–33].

Moreover, Koenderink and van Doorn [38,39] considered the problem of deriving linear operators from the scale-space representation considering that size invariance and the absence of spurious resolution are two requirements that characterize well-behaved spatial sampling in visual systems. They concluded that these operators must obey the time-independent Schrödinger equation, that is, a physical equation that governs the quantum mechanical oscillator. Thus, they provided a formal statement that Gaussian derivatives are *natural operators* to derive from scale-space.

The HT was originally developed as a mathematical model for explaining the receptive fields during early stages of human vision [40,41]. It is a special case of polynomial transforms whose basis functions are derivatives of Gaussian functions. The extension of this model to the multiresolution case was then formulated [42,43].

The HT uses overlapping Gaussian windows and projects images locally onto a basis of orthogonal polynomials.

First, windowing with a local function $\omega(x-p, y-q)$ at positions p, q that conform the sampling lattice S takes place. As argued before, the scale-space suggests using a Gaussian window, that is,

$$\omega(x,y) = \frac{1}{2\pi\sigma^2}\exp\left(-\frac{(x^2+y^2)}{2\sigma^2}\right) \tag{24.1}$$

where σ is spread of the Gaussian window.

The Gaussian window is separable into Cartesian coordinates; it is isotropic, thus, it is rotationally invariant.

Through the replication of the window function over the sampling lattice, a periodic weighting function is defined as $W(x,y) = \sum_{(p,q)\in S}\omega(x-p, y-q)$. This weighting function must be different from zero for all coordinates (x, y). Next, local information at each analysis window is expanded in terms of a family of orthogonal polynomials $G_{m,n-m}(x, y)$ of the order m in x and $n-m$ in y. They are determined by the analysis window function, and satisfy the orthogonal condition:

$$\int_{-\infty}^{+\infty}\int_{-\infty}^{+\infty}\omega^2(x,y)G_{m,n-m}(x,y)G_{l,k-l}(x,y)\,\mathrm{d}x\mathrm{d}y = \delta_{nk}\delta_{ml} \tag{24.2}$$

Q2, Q3 for $n, k = 0,\ldots\ldots;\infty$, $m = 0, n$ and $l = 0, k$; where δ_{nk} denotes the Kronecker function.

In the case of a Gaussian window function, the associated orthogonal polynomials are the Hermite polynomials:

$$G_{n-m,m}(x,y) = \frac{1}{\sqrt{2^n(n-m)!m!}}H_{n-m}\left(\frac{x}{\sigma}\right)H_m\left(\frac{y}{\sigma}\right) \tag{24.3}$$

where $H_n(x)$ denotes the nth Hermite polynomial of degree n in x [44].

The polynomial coefficients $L_{m,n-m}(p, q)$ are calculated by convolution of the original image $L(x, y)$ with the filter function:

$$D_{m,n-m}(x,y) = G_{m,n-m}(-x,-y)\omega^2(-x,-y) \tag{24.4}$$

followed by subsampling at positions (p, q) of the sampling lattice S. For the case of the Hermite transform, it can be shown [40] that the filter functions $D_{m,n-m}(x, y)$ correspond to Gaussian derivatives of order m in x and $n-m$ in y, in agreement with the Gaussian derivative model of early vision.

The process of recovering the original image (synthesis) consists of interpolating the transform coefficients with the proper synthesis filters. This process is called an inverse polynomial transform and is defined by

$$\hat{L}(x,y) = \sum_{n=0}^{N}\sum_{m=0}^{n}\sum_{(p,q)\in S}L_{m,n-m}(p,q)P_{m,n-m}(x-p,\ y-q) \tag{24.5}$$

The synthesis filters $P_{m,n-m}(x,y)$ of order m and $n-m$ are defined by

$$P_{m,n-m}(x,y) = \frac{G_{m,n-m}(x,y)\omega(x,y)}{W(x,y)}$$

for $m = 0, \ldots, n$ and $n = 0, \ldots, \infty$.

In a discrete implementation, the Gaussian window function may be approximated by the binomial window function $\omega^2(x) = (1/2^N)C_N^x$ for $x = 0, \ldots, N$, where N is called the order of the binomial window and represents the function length, and $C_N^x = N!/(N-x)!x!$ for $x = 0, \ldots, M$. In this case, the orthogonal polynomials $G_{m,n-m}(x, y)$ associated with the binomial window are known as the Krawtchouck's polynomials:

$$K_n[x] = \frac{1}{\sqrt{C_N^n}} \sum_{k=0}^{n} (-1)^{n-k} C_{N-x}^{n-k} C_x^k$$

for $n = 0, 1, \ldots, N$

For this discrete case, all previous relations hold, with some interesting modifications. First, support of the window function is finite (N); as a consequence, expansion with the Krawtchouck polynomials is also finite, and signal reconstruction from the expansion coefficients is perfect.

To define a polynomial transform, some parameters have to be chosen. First, we have to define the characteristics of the window function. As argued before, the Gaussian window is the best option from a perceptual point of view and from the scale-space theory, however, a discrete implementation may call for a discrete transform, and in this case the binomial window is a good choice. Another important parameter is the window spread. The choice may depend on the scale-space representation of the target objects in the image. Fine local changes are better detected with small windows, but on the contrary, representation of low-resolution objects need large windows. We have chosen binomial windows of orders $N = 2$; however, in order to overcome spatial resolution compromises, multiresolution representations are a good solution [42,43].

Last but not least, the subsampling factor, is a free parameter directly related to the subsampling positions (p, q) of the sampling lattice S. From a mathematical point of view, the only constraint for this parameter is that the weighting function $W(x, y)$ must be different from zero for all coordinates (x, y). In the case of the binomial window, for instance, this constraint translates into subsampling factors ranging from 1 to N. It can be noted that changing this subsampling factor will only produce different synthesis filters; analysis filters remain the same. A subsampling factor of 1 produces nondecimated image decompositions, which are known to yield shift invariance and are highly valuable for image reconstruction problems such as fusion. Larger subsampling factors produce decimated decompositions that in the case of pyramidal multiresolution schemes are computationally efficient. Figure 24.1a shows a Hermite transform decomposition. The original image is decomposed into a number of subimages which consist of a low-pass (approximation) image known as zero-order coefficient ($L_{0,0}$) and a series of high-pass coefficients containing detailed information. Figure 24.1a depicts coefficients of order zero ($L_{0,0}$), up to order three ($L_{2,1}$) and ($L_{1,2}$).

24.2.2 The Steered Hermite Transform

The Hermite transform has the advantage that high-energy compaction can be obtained through adaptively steering the transform [19,20]. The term "steerable filters" describes a set of filters that are rotated copies of each other, and a copy of the filter in any orientation which is then constructed as a linear combination of a set of basis filters [45]. The resulting transform is self-inverting and translation- and rotation-invariant. Based on the steering property, the Hermite filters at each position in the image adapt to the local orientation content. This adaptability results in significant information compaction. The local rotation into the domain transform can be seen like a mapping of the

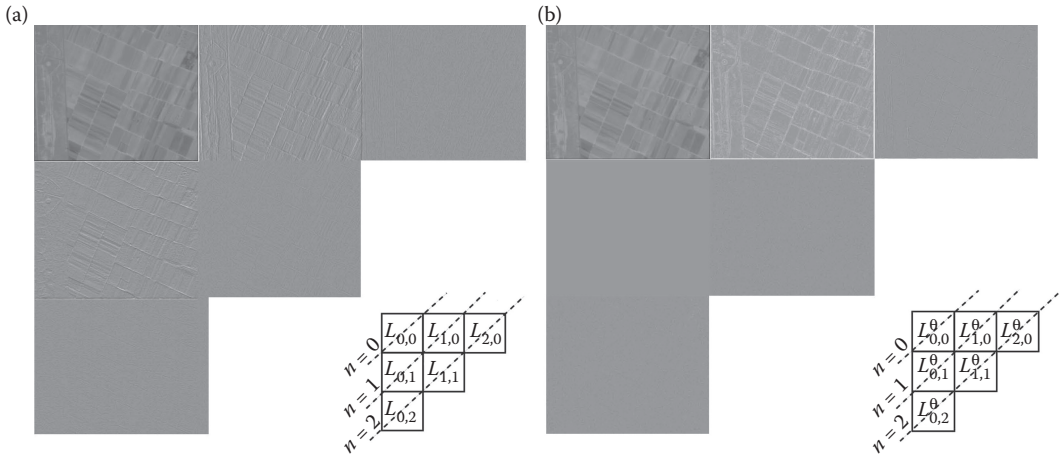

FIGURE 24.1 Decimated Hermite transform. Left: Original Hermite coefficients of image depicted in Figure 24.7a. Diagram shows the coefficient orders. Diagonals depict zero-order coefficients ($n = 0$), first-order coefficients ($n = 1$), and so on. Binomial window of order $N = 2$ and a subsampling factor of 2 were used. Right: Steered coefficients toward the local gradient angle. It can be noted that most coefficient energy is concentrated on the upper row of the steered coefficients and that coefficient $L^{\theta}_{1,0} = 0$.

expansion coefficients into a local coordinate system whose main axis corresponds to the direction of maximal signal energy. Rotation of the filter functions can be obtained by

$$D_{n-m,m}(x,y,\theta) = \sum_{k=0}^{n} \alpha_m(k,n,\theta) D_{k,n-k}(x,y)$$

where $\alpha_n(k,N,\theta) = s^k c^{-k} \Delta^n \{C_{N-n}^{k-n} c^{2k-n} s^{N-2k+n}\}$
for k, $n = 0, \ldots, N$; $N \in \mathbb{N}$; and $c = \cos\theta$, $s = \sin\theta$,
for $\theta \in [0, 2\pi)$.

Orientation θ of local maximum energy can be estimated by maximizing the coefficient energy measure at each window position. Furthermore, the steered Hermite transform offers a way to estimate one-dimensional (1D) energy,

$$E_N^{1D}(\theta) = \sum_{n=1}^{N} \left[L^{\theta}_{n,0} \right]^2$$

and 2D energy,

$$E_N^{2D}(\theta) = \sum_{n=1}^{N} \sum_{m=1}^{n} \left[L^{\theta}_{n-m,m} \right]^2.$$

By analyzing relations between these energies, it is possible to classify image patterns. Figure 24.2 shows a dimensional pattern classification obtained from a natural scene [42].

In practice, the local gradient angle, calculated from the expansion coefficients as $\theta = \arctan L_{0,1} / L_{1,0}$, where $L_{0,1}$ and $L_{1,0}$ are the first-order coefficients of the Hermite transform, can be an alternative estimator of the rotation angle θ. This choice would imply $L^{\theta}_{1,0} = 0$, as can be noted in Figure 24.1b.

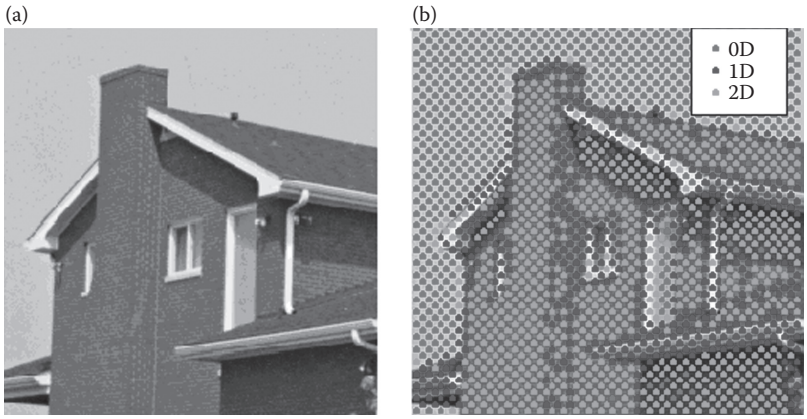

FIGURE 24.2 0D, 1D, and 2D patterns found in a natural scene from dimensional energy analysis with the rotated Hermite transform. **Q4**

24.3 FUSION METHOD BASED ON THE HERMITE TRANSFORM

24.3.1 Fusion Scheme with Multispectral and Panchromatic Images

Our objective in image fusion is to generate synthetic images that preserve the higher spatial resolution of the panchromatic (PAN) images while keeping the spectral characteristics of the original multispectral (MS) data.

In a way similar to other fusion techniques, our proposed fusion method requires that the multispectral images be resampled so that their pixel size will be the same as that of the panchromatic image.

The general framework for multispectral and panchromatic image fusion with the Hermite transform consists of several steps [46,47]:

I. Generate new panchromatic bands, whose histograms match each multispectral band's histogram. The purpose of doing this is that each pair of images has the same mean and standard deviation.

II. Perform Hermite transform decomposition over each of the two images, MS and PAN. The decompositions consist of a number of several subimages which represent a low-pass residue known as zero-order coefficients ($L_{0,0}^{MS}$ and $L_{0,0}^{PAN}$) and several high-pass bands containing detailed information coefficients: $L_{0,1}^{MS}$ and $L_{1,0}^{MS}$, and $L_{0,1}^{PAN}$ and $L_{1,0}^{PAN}$ are the first-order coefficients for the MS and PAN images; $L_{0,2}^{MS}$, $L_{1,1}^{MS}$ and $L_{2,0}^{MS}$, $L_{0,2}^{PAN}$, $L_{1,1}^{PAN}$ and $L_{2,0}^{PAN}$ are the second-order coefficients for the MS and PAN images, respectively, and so on, until the highest coefficient order N. For practical reasons, we implemented the discrete Hermite transform which, in fact, as argued before, uses a binomial window function of order N, and corresponding orthogonal polynomials known as Krawtchouck's polynomials. Theoretical and practical issues about this discrete polynomial transform have been well studied [42,43,48]. It is well known that the binomial function of order N approximates a Gaussian function with spread $\sigma = \sqrt{N/2}$. N also represents the maximum order of the transform coefficients since the binomial function has compact support. As explained in the previous section, the subsampling factor, this is, the distance between adjacent window functions is a free parameter. We found just perceivable, but significant, differences in fusion performance when setting this parameter to different values, and chose to fix this parameter to both its maximum allowed value, that is, N, and its minimum value, that is, one pixel. The former provides decimated

structures with less computational complexity, while the latter produces nondecimated shift-invariance decompositions.

III. Locally rotate the HT coefficients toward the direction of maximum of energy. As previously explained, rotation angle can also be estimated by the local gradient angle. The steered Hermite transform has the advantage of energy compaction. Transform coefficients are selected with an energy compaction criterion from the steered Hermite transform; therefore, it is possible to reconstruct an image with few coefficients and still preserve details such as edges and textures. Hence, a set of rotated coefficients, that is, $L_{n,m}^{MS^{\theta}}$ and $L_{n,m}^{PAN^{\theta}}$ are obtained for the MS and PAN images, respectively.

IV. Select high-pass transform coefficients from each set (MS and PAN), according to a fusion rule based on the verification of consistency methods (Li et al. 1995) [49]. This approach considers the maximum absolute value within a 5×5 window over the image (area of activity). Increasing the size of the window may cause problems with lower salient patterns. The window variance is used as a measurement of the activity associated with the central pixel of the window. At each window position the maximum selection rule is used so that a significant value indicates the presence of a dominant pattern in the local area. A map of binary decision is then created and subjected to verification of consistency based on a majority filter in order to correct wrong selections. In practice, reconstruction can be achieved with a small number of coefficients, specifically those with high energy of compaction, that is, the upper-row coefficients as shown in Figure 24.1b, this to say $L_{1,0}^{MS^{\theta}}$, $L_{2,0}^{MS^{\theta}}$ and $L_{3,0}^{MS^{\theta}}$, …, $L_{1,0}^{PAN^{\theta}}$, $L_{2,0}^{PAN^{\theta}}$ and $L_{3,0}^{PAN^{\theta}}$ … for the MS and PAN images, respectively. This is especially true for the case of one-dimensional patterns whose components are all concentrated in these coefficients. Texture patterns may indeed need all coefficients for perfect reconstruction; however, differences are little noticeable.

Q5

V. Add these new set of high-pass combined coefficients $L_{1,0}^{fus^{\theta}}$, $L_{2,0}^{fus^{\theta}}$, and $L_{3,0}^{fus^{\theta}}$ to the zero-order coefficient obtained from the MS ($L_{0,0}^{MS}$) image, in order to create a new transform coefficient set that corresponds to the fused image.

VI. Finally, perform an inverse Hermite transform over the new rotated coefficient set.

Steps II through VI are repeated for each multispectral band.

Figure 24.3 shows a scheme of the proposed fusion method. This is executed band by band.

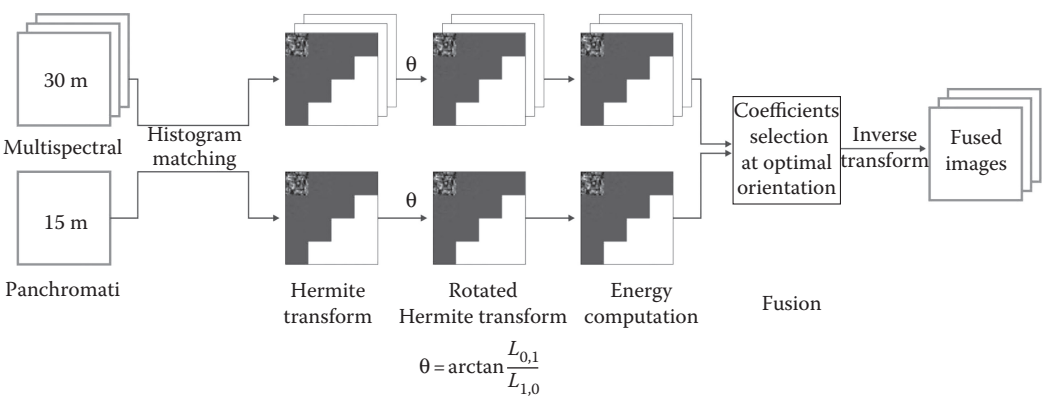

FIGURE 24.3 Hermite transform fusion method for multispectral and panchromatic images.

24.3.2 Fusion Scheme with Multispectral Images and SAR Image

The use of synthetic aperture radar (SAR) images as a complement to visible and multispectral images is becoming increasingly popular because of their capability of imaging even in the case of cloud-covered remote areas.

Unfortunately, the poor quality of SAR images makes it very difficult to perform direct information extraction tasks. Numerous filters have been proposed to remove speckle in SAR imagery; however, in most cases and even in the most elegant approaches, filtering algorithms have a tendency to smooth speckle as well as information. For numerous applications, low-level processing of SAR images remains a partially unsolved problem.

A wide variety of transform-based methods for speckle reduction have been proposed in the literature. Donoho and Johnstone [50,51] proposed to apply a threshold (T) to the wavelet detail coefficients. This nonlineal technique is fairly simple and implies the use of a binary decision map. Wavelet coefficient handling consists of keeping (or shrinking) and discarding (or killing) the coefficient. There are two alternatives for this scheme, hard thresholding and soft thresholding [52]. Let us assume that U is the coefficient value and D is the resulting coefficient value after thresholding. Hard thresholding is defined by $D(U,T) = U$ for all $|U| > T$, $D(U,T) = 0$ otherwise. This is known to account for a MIN-MAX binary decision solution. Soft thresholding is implemented by $D(U,T) = \text{sgn}(U)\max(0,|U| - T)$. In this case, coefficients are shrunk if their absolute value exceeds the threshold. The universal threshold proposed by Donoho and Johnstone [51] is defined by $T_{\text{universal}} = \sigma_n\sqrt{2\log(M)}$, where M is the sample size, and σ_n is the noise standard deviation. The universal threshold has been recognized as simple and efficient, especially when signal characteristics are unknown; however, it does not allow local adaptation. An alternative way to compute a suitable threshold has been proposed by Chang et al. [53], based on a minimum mean-square error criterion (MMSE). This method, called Bayes–Shrink, computes a signal-dependent threshold as $T = \sigma_n^2/\sigma_x^2$, where σ_n^2 y σ_x^2 are the local noise and signal variance, respectively. An adaptation of this method to speckle reduction with the undecimated wavelet transform was done by Argenti and Alparone [54]. Q6

We propose a method for thresholding the Hermite transform coefficients that locally adapts to the mean luminance value, thus compensating the multiplicative nature of speckle. Thresholding occurs only in homogeneous regions. According to the central limit theorem, the probability density function of transformed coefficients belonging to noisy homogeneous regions (i.e., in absence of image structures) approaches a Gaussian distribution. This means that the solution of MIN-MAX and MMSE detection criteria are equivalent. Our approach radically differs in the way noisy edges are treated. In this case, the rotated Hermite transform detects the orientation of edges, so that when edges are reconstructed, only those coefficients aligned with the corresponding edge orientation are included. All other coefficients are set to zero, thus eliminating the structure of speckle on edges, while preserving sharpness.

24.3.3 Noise Reduction with the Hermite Transform

The Hermite transform coefficients can be used to discriminate noise from relevant information such as edges and lines in SAR imagery [55,56]. A binary decision mask containing relevant image locations is built by properly thresholding (T) the first-order transform coefficient energy E_1: $E_1 = L_{0,1}^2 + L_{1,0}^2$ where $L_{0,1}$ and $L_{1,0}$ are the first-order coefficients of the Hermite transform.

As explained before, these coefficients are obtained by convolving the original image with the first-order derivatives of a Gaussian function, which are known to be quasi-optimal edge detectors; therefore, the first-order energy can be used to discriminate edges from noise by means of a threshold scheme.

The mask is then defined by

$$\text{Mask} = \begin{cases} 0 & \textit{if} \quad E_1 < T \\ 1 & \text{otherwise} \end{cases}$$

The optimal threshold is set considering two important characteristics of SAR images. First, one-look amplitude SAR images have a Rayleigh distribution and the signal-to-noise ratio (SNR) is ~1.9131. Second, in general, the SNR of multilook SAR images does not change over the whole image.

The threshold is calculated by

$$T = \frac{2\alpha}{\text{SNR}^2 N_{\text{look}}} \ln\left(\frac{1}{\text{Pr}}\right) L_{00}^2$$

- SNR is the signal-to-noise ratio, equal to 1.9131
- N_{look} is the number of looks of the image.
- $\alpha = \left| R_L(x,y) * D_{1,0}(x,y) * D_{1,0}(-x,-y) \right|_{x=y=0}$, R_L is the normalized autocorrelation function of the input noise, and $D_{1,0}$ is the filter used to calculate the first-order coefficient.
- P_{R} is the probability (percentage) of noise left on the image and will be set by the user.
- L_{00} is the zero-order Hermite coefficient.

A careful analysis of this expression reveals that this threshold adapts to the local content of the image because of the dependence of σ on the local mean value μ_l, the latter being approximated by the Hermite coefficient L_{00}.

With the locations of relevant edges detected, the next step is to represent these locations as one-dimensional patterns. This can be achieved by steering the Hermite transform as described in the previous section so that the steering angle θ is determined by the local edge orientation. Next, only coefficients $L_{n,0}^{\theta}$ are preserved; all others are set to zero. This strategy is extremely effective for the restoration of noisy edges, since only oriented features are considered for edge reconstruction. An alternative interpretation of this strategy is that edge reconstruction is achieved by projecting edge transform coefficients over a one-dimensional space spanned toward the edge orientation. Two-dimensional structures, as is the case of noise located on edges, are thus eliminated.

In summary, the noise reduction strategy consists of classifying the image in either zero-dimensional patterns consisting of homogeneous noisy regions, or one-dimensional patterns containing noisy edges. The former are represented by the zero-order Hermite transform, that is, the local mean value, and the latter by oriented 1D Hermite coefficients.

When an inverse Hermite transform is performed over these selected coefficients, the resulting synthesized image consists of noise-free sharp edges and smoothed homogeneous regions. Therefore, the denoised image preserves sharpness and thus, image quality. Some speckle remains in the image since there is always a compromise between the degree of noise reduction and the preservation of low-contrast edges. The user controls the balance of this compromise by changing the percentage of noise left P_{R} on the image according to Equation 24.18. Figure 24.4 shows the algorithm for noise reduction.

24.3.4 Image Fusion

It is easy to figure out that local orientation analysis for the purpose of noise reduction can be combined with an image fusion scheme as the one described in Section 24.4.1. Figure 24.5 shows the complete methodology to reduce noise and fuse Landsat 7 TM with SAR images. After noise

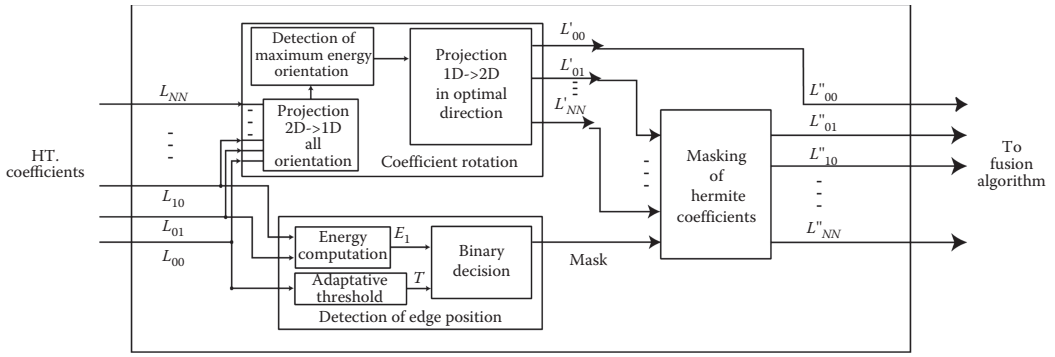

FIGURE 24.4 Noise reduction algorithm.

reduction is applied to the SAR image, histogram matching is applied on this image to adjust mean values with each MS band. With a similar method as the one previously described, a new coefficient set is generated, consisting of $L^{MS}_{0,0}$ and the detail coefficients selected either from the SAR or MS images. Finally, an inverse transform is performed to obtain the fused image.

24.4 EXPERIMENTAL RESULTS

As explained before, we use a discrete implementation of the Hermite transform based on a binomial filter of order N, and its corresponding orthogonal Krawtchouck's polynomials. We obtained best fusion performance with binomial window functions of orders $N = 2$.

24.4.1 Multispectral and Panchromatic Image Fusion

In this section, we show the results of image fusion with decimated and undecimated versions of the Hermite transform, and compare their performance with the well-known eFIHS [17] and AWL methods [12]; both have become widely accepted since they have overcome several of the limitations of traditional wavelet schemes. The proposed fusion scheme images have been tested on optical data, namely multispectral images from SPOT 5 (10 m spatial resolution and spectral ranges: B1 green 0.50–0.59 μm, B2 red 0.61–0.68 μm, B3 NIR 0.78–0.89 μm spectral range) and its panchromatic band (2.5 m resolution spatial, 0.48–0.71 μm spectral range). They were acquired on January 01, 2007.

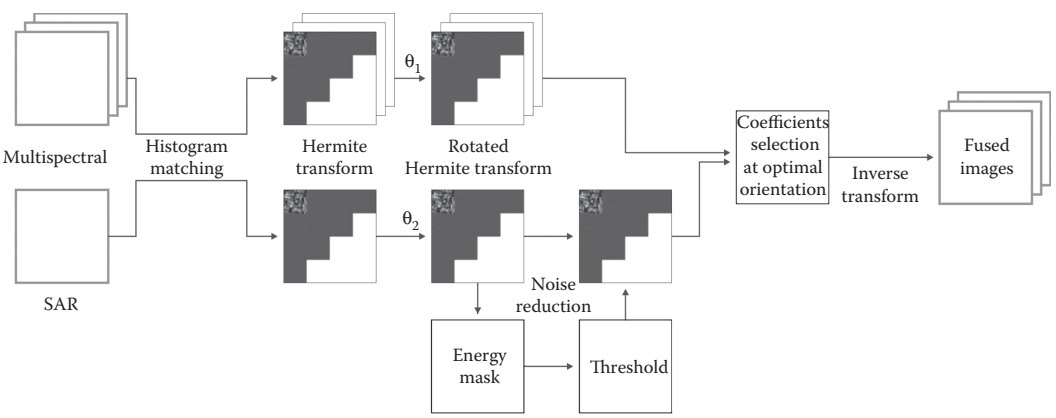

FIGURE 24.5 Noise reduction and fusion for multispectral and SAR images.

Comparison of the proposed methods was based on spectral quality index [10] and spatial quality [9], Moreover, red versus NIR dispersion diagrams were also analyzed which are useful for biophysical variable interpretation [22,57,58].

24.4.1.1 Visual Quality

Figure 24.6 shows an amplified (zoom) area of a fused image using decimated and undecimated HT
Q7 schemes. $N = 2$ for both cases. It can be clearly seen that image reconstruction is better for the case of the undecimated HT. This is especially true for one-dimensional structures, such as edges and lines. This might be due to the shift invariance property of the undecimated HT. Figure 24.6 also shows a comparison of the HT results with the eFIHS and AWL methods. In this case too, the undecimated HT outperforms the eFIHS since it provides sharper performance, thus higher spatial resolution. This might be explained by the local orientation analysis performed within the HT meth-

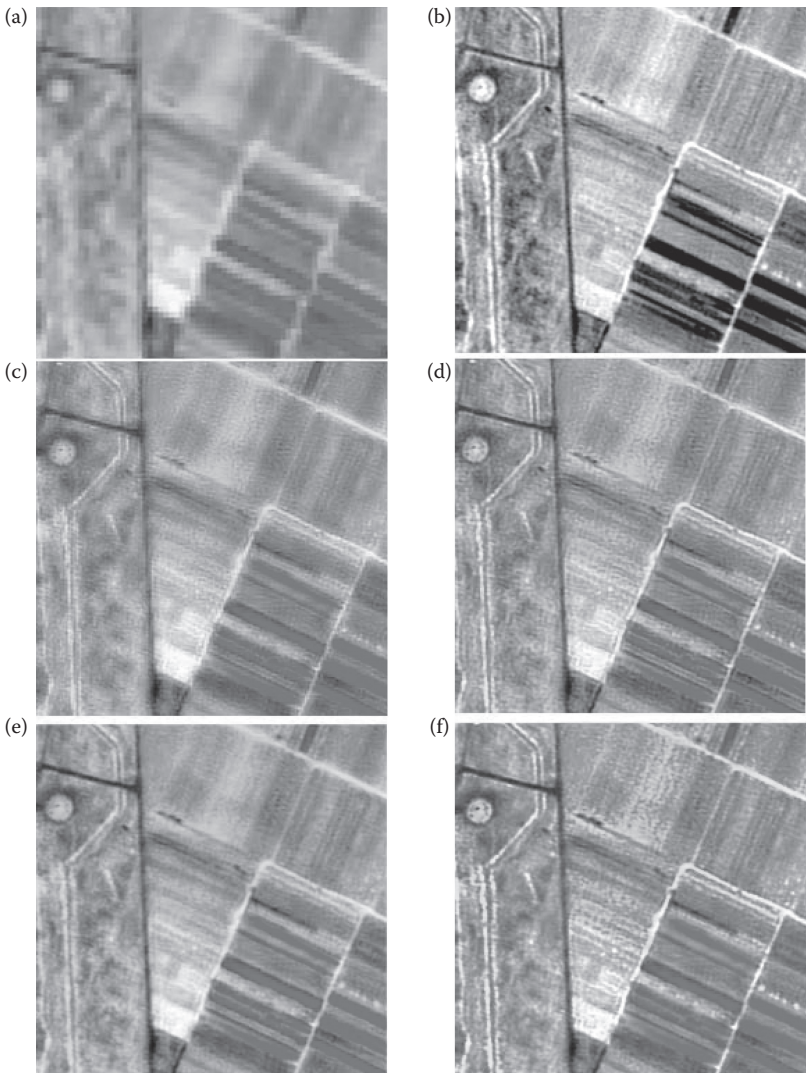

FIGURE 24.6 (**See color insert.**) (a) Multispectral SPOT 5 image (original 10 m). (b) Panchromatic SPOT 5(2.5 m). (c) Fusion result with the decimated HT method ($N = 2$). (d) Fusion result with the undecimated HT ($N = 2$). (e) Fusion with eFIHS. (f) AWL false color composite scheme for displaying SPOT multispectral images is achieved with R = XS3 (NIR band), G = XS2 (red band), and B = XS1 (green band).

odology. The undecimated HT and the AWL methods show similar performance from a subjective point of view. Both present sharp results with similar spatial content.

24.4.1.2 Spectral Quality and Spatial Quality

Digital values were converted to spectral radiance units, measured in watts per square meter per steradian per micron (W/m^2 sr μm).

Spectral quality of a fused image can be assessed with respect to a reference image [2,10]. A new set of low-resolution images were created from the original multispectral and panchromatic images. Spatial resolution was reduced to about half the original value. A Gaussian filter was used for this purpose. The original multispectral image served as reference image B_k. The different fusion methods are then applied to the set of low-resolution images and the resulting images are then compared to reference image B_k.

Different objective quality metrics were calculated for all fused products with respect to the reference image B_k, namely the correlation coefficient, the difference mean value (bias), and the standard deviation of the difference image (sdd). Another quality metric for fused products, the ERGAS, was also calculated. ERGAS stands for *erreur relative globale adimensionnelle de synthese*, and is an estimator of the global spectral quality of fused products:

$$\text{ERGAS} = 100\frac{h}{l}\sqrt{\frac{1}{N}\sum_{k=1}^{N}\left(\frac{\text{RMSE}\left(B_k\right)^2}{\left(M_k\right)^2}\right)} \tag{24.6}$$

where RMSE is the root mean square error, defined by

$$\text{RMSE}\left(B_k\right) = \sqrt{\left(\text{bias}\right)^2 + \left(\text{sdd}\right)^2},$$

where h is the resolution of the panchromatic image, l the resolution of multispectral images, S the number of spectral bands, B_k the reference spectral image, and M_k the mean value of the reference image B_k.

Ideally, both bias and the difference of standard deviations should tend to null, and the correlation coefficient should tend to one. The closer to zero an ERGAS value the better the image quality. Table 24.1 shows all these quality metrics for all fused methods, including the discrete Hermite transform. Results of Table 24.1 are presented for each multispectral band B1 to B3, in spectral radiance units. It can be noted that the best performance is achieved by the undecimated HT.

TABLE 24.1
Comparison of Spectral Quality Metrics for Different Fusion Methods

	Spectral Quality			
Correlation	**AWL**	**eFIHS**	**HT**	**uHT**
B1	0.9790	0.9735	0.9791	0.9845
B2	0.9890	0.9855	0.9792	0.9846
B3	0.9918	0.9918	0.9634	0.9920
ERGAS	1.9801	2.2071	2.2191	2.0628
	Spatial Quality			
B1	0.940	0.943	0.929	0.939
B2	0.934	0.932	0.923	0.945
B3	0.920	0.926	0.919	0.947

In order to estimate the spatial quality, an objective method proposed by Zhou et al. (1988) was used. A Laplacian filter is applied to all fusion products to be compared, as well as to the original panchromatic image. Then, correlation coefficients between each Laplacian-filtered fused image and original panchromatic image are calculated.

In this case too, undecimated HT outperforms decimated HT as well as eFIHS methods Once again, AWL and undecimated HT perform very similarly with no significant differences in these parameters.

24.4.1.3 Red Versus NIR Dispersion Diagrams

The determination of spectral quality of the fused images is a complex task. Besides the spectral quality indexes presented before, we present next an analysis of parameters that describe soil line, and patterns of absorption/reflectance that represent relations between red and NIR. Due to the linear relation between red and NIR reflectance that describes the soil line, these parameters have been shown to be of major importance for the interpretation of remote sensed data [57]. Some studies refer to the importance of the soil line to extract relevant biophysical variables such as the leaf area index (LAI) [58].

In this work, we obtained the soil line parameters from the red–NIR spectral space as described in Ref. [22].

Soil line was obtained with the formula $\rho_{NIR} = \alpha/\rho_R + \beta$, where ρ_R and ρ_{NIR} are the reflectance in red and near-infrared bands, and α and β are the slope and intercept of the soil line.

Because many investigations have inferred vegetation measurements from near-infrared (NIR) and red data, we analyzed the integrity of information content before and after the fusion procedure. At first glance, little difference in the scatter plots is found between the different fusion methods with respect to the original. However, a deeper analysis shows relevant deviations of the eFIHS and the decimated HT methods. Soil line parameters were extracted from red and NIR data (Table 24.2) and plotted in Figure 24.7. Soil line plots show that undecimated HT and AWL remain very close to the original data, while the decimated HT slightly deviates from the original slope. The eFIHS slope remains close to the original; however, it deviates from its intercept, and its minimum and maximum reflectances also deviate considerably from the original data, meaning more substantial changes in spectra content with respect to the original multispectral data.

24.4.2 Multispectral and SAR Image Fusion

An interesting application of image fusion is to integrate information from different sensors, namely multispectral (MS) and synthetic aperture radar (SAR) images.

Despite the fact that MS and SAR images retrieve different kinds of information, it has been proved that the combination of both sources provides a means to better identify features in the scene. Recently, MS and SAR image data integration has been proposed by Alparone et al. [21].

TABLE 24.2
Soil Line Parameters Extracted from the Red–NIR Space of Different Fusion Methods

Fusion Method	α	β	Minimum Reflectances of Soil	Maximum Reflectances of Soil
Original	1.1758	0.0078	(0.0647,0.0839)	(0.1437,0.1768)
uHT	1.1591	0.0082	(0.0643,0.0818)	(0.1428,0.1727)
HT	1.1195	0.0049	(0.0639,0.0792)	(0.1419,0.1670)
eFIHS	1.1982	0.0036	(0.0581,0.0732)	(0.1604,0.1957)
AWL	1.168	0.0078	(0.06475,0.007811)	(0.1316,0.1682)

Note: α, slope; β, intercept.

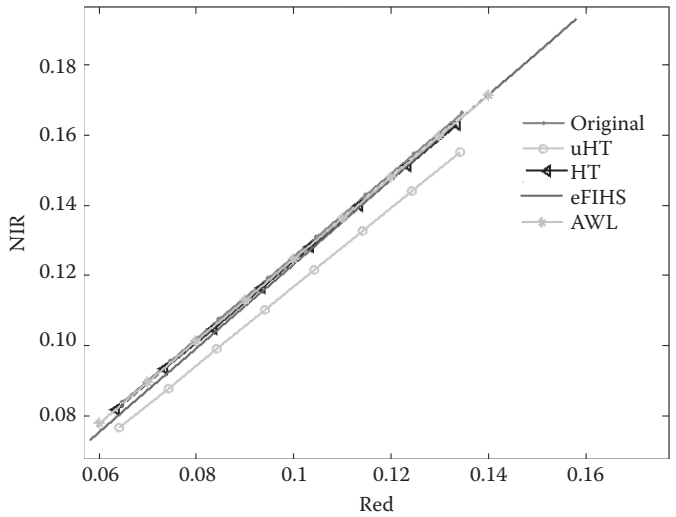

FIGURE 24.7 Soil line in red and NIR bands obtained from different fusion methods.

Here, a generalized intensity modulation (GIM) fusion scheme is proposed in combination with an IHS wavelet à trous transform. This method is capable of fusing MS, P, and SAR images within the same scheme. Detail information from an SAR image is injected in a multiplicative scheme, while P detail information is included within an additive model. This method assumes that noise on the SAR image has been previously reduced.

Our proposed fusion scheme integrates MS and SAR image information. As explained before, the Hermite transform is used with a double purpose, fuse image information and reduce speckle in the SAR image.

Landsat 7 TM 30 m spatial resolution and spectral ranges B1 (0.45–0.52 μm), B2 (0.52–0.60 μm), B3 (0.63–0.69 μm), B4 (0.76–0.90 μm), B5 (1.55–1.76 μm), B7 (2.08–2.35 μm), and SAR AeS-1 (5 m resolution spatial) images were used in this study. Landsat 7 ETM+ data was obtained on January 11, 2001, orbit 2647. AeS-1 data was acquired between October 1998 and January 1999.

We fused both sensor images with the Hermite transform and compared results with the GIM method [21]. GIM did not include a panchromatic image, only the Landsat and Radarsat images were fused as shown in Figure 24.8. Moreover, in order to make a fair comparison, speckle reduction with the Hermite transform was also applied to the SAR AeS-1 image before GIM fusion.

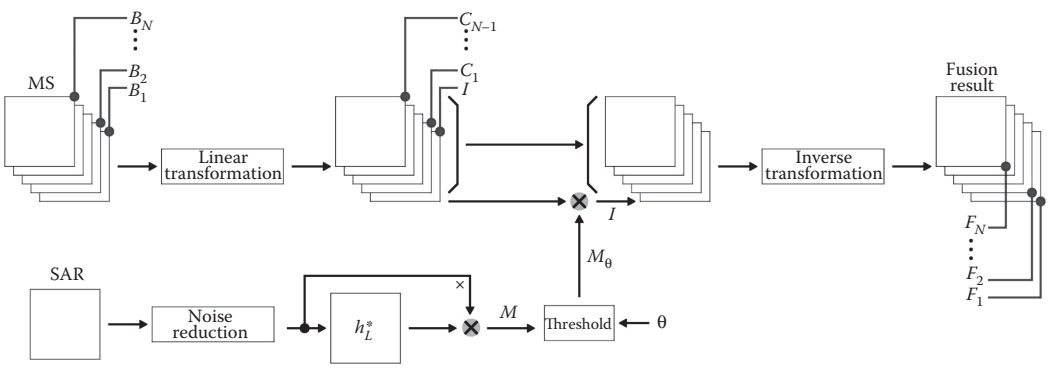

FIGURE 24.8 Modified GIM fusion algorithm.

24.4.2.1 Visual Quality

Figure 24.9 illustrates the result of multispectral and SAR image fusion with the uHT and GIM methods. SAR images contain higher spatial resolution and more texture than MS images. In contrast, the former contain spectral information. Fusion results show that all these properties can be well incorporated into a single product. uHT- as well as GIM-fused images show significant spatial resolution improvement with respect to the original MS image, while no apparent spectral information is lost. The uHT, however, shows sharper results, better image structure reconstruction, and more natural texture content. This can be easily noted in the airport landing track and in the river contours.

24.4.2.2 Spectral Quality

The spectral angle mapper (SAM) is a measure of the spectral distortion and is defined as the absolute angle between the two vectors: $\mathrm{SAM}(v, \hat{v}) = \arccos(\langle v, \hat{v}\rangle / \| v \|_2 \cdot \| \hat{v} \|_2)$, where $v = \{v_1, v_2, \ldots v_N\}$ is the original spectral vector and $\hat{v} = \{\hat{v}_1, \hat{v}_2, \ldots \hat{v}_N\}$ is the spectral vector obtained after fusion. Table 24.3 shows that the undecimated HT presents a 0.5° larger SAM than GIM.

24.4.2.3 Classification

In order to evaluate the algorithm performance in real applications, original and fused images were classified with the ISODATA algorithm in four different classes. Figure 24.10 shows the results of this experiment. Deforested and vegetation classified areas are difficult to evaluate, since a ground truth is not available; however, the river and the airport landing track are easily identified in the fused images. In both cases, the uHT transform clearly separates classes more efficiently than GIM. It is important to note that the landing track high-resolution image primitives were not present in the original MS image but were injected from the SAR image.

24.5 CONCLUSIONS

In this chapter, we presented the Hermite transform as an efficient tool for image fusion in remote sensed data. The use of Gaussian derivatives as basis functions of the HT makes this transform especially suitable to represent relevant image structures such as edges. Moreover, the rotation

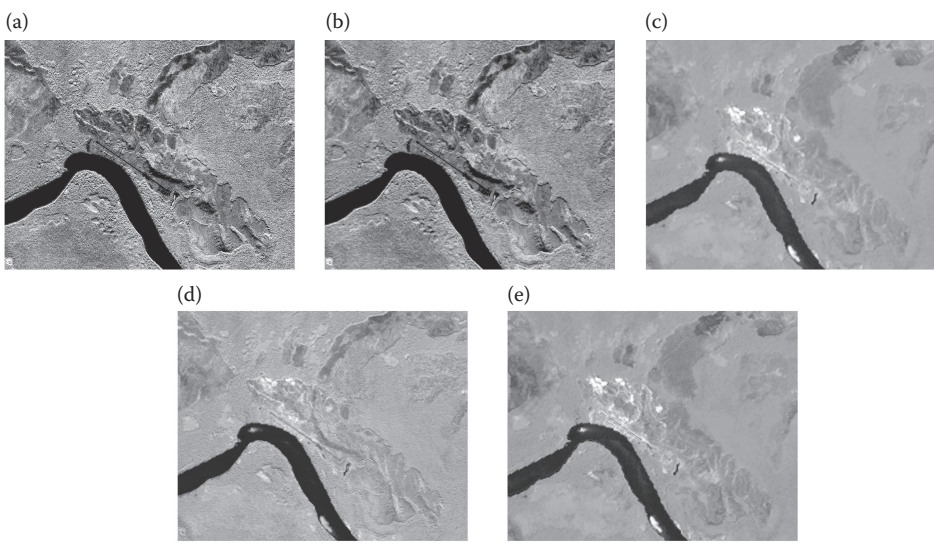

FIGURE 24.9 (**See color insert.**) (a) Original SAR AeS-1 images with speckle. (b) SAR AeS-1 restored image. (c) Landsat 7 TM image. (d) uHT fused image. (e) GIM fused image.

TABLE 24.3
Spectral Distortion

Fusion Methods	uHT	GIM	Ideal
SAM	5.41°	4.89°	0°

Note: Average SAM between resampled original and fused image for both uHT and GIM methods.

property of the Hermite transform presented here is an important feature that allows detecting the orientation of relevant image structures. This translates into an energy compaction into few coefficients of the transform. Furthermore, the local orientation property of the HT is a key factor for the reconstruction of oriented patterns. We profit from this property in the proposed speckle reduction algorithm for SAR images. While noise in homogeneous regions is reduced by means of a local adaptive threshold scheme, noise present on edges is reduced by reconstructing them from transform coefficients that are oriented toward the proper edge direction. Another very important feature of the Hermite transform is the freedom to choose the subsampling factor used to compute the transform coefficients, the analysis window length being the only constraint. This implies that decimated and undecimated Hermite transform structures can be very easily generated by just changing a single parameter. This is especially relevant for the construction of shift invariant image analysis structures.

We presented two fusion methodologies, one for multispectral and panchromatic images, and the other for multispectral and SAR images. In the first case, fused products showed how to efficiently preserve the higher spatial resolution of the P image and the spectral content of the MS image. Evaluation was performed taking into account visual quality, spectral quality, and biophysical variable integrity. In all cases, the undecimated Hermite transform outperformed the eFIHS method and performed as well as AWL, both being two of the most referenced fusion methods in the recent literature. The proposed scheme for fusion between MS and SAR images also shows very good performance, since the higher resolution and relevant texture of the SAR image is incorporated into the MS image without losing spectral integrity. Noise reduction is a key factor in this case, since it is of extreme importance not to incorporate spurious information to the fused product. Comparison with the generalized intensity modulation fusion algorithm shows a better performance of the undecimated Hermite transform in terms of visual quality and spatial reconstruction. Analysis by

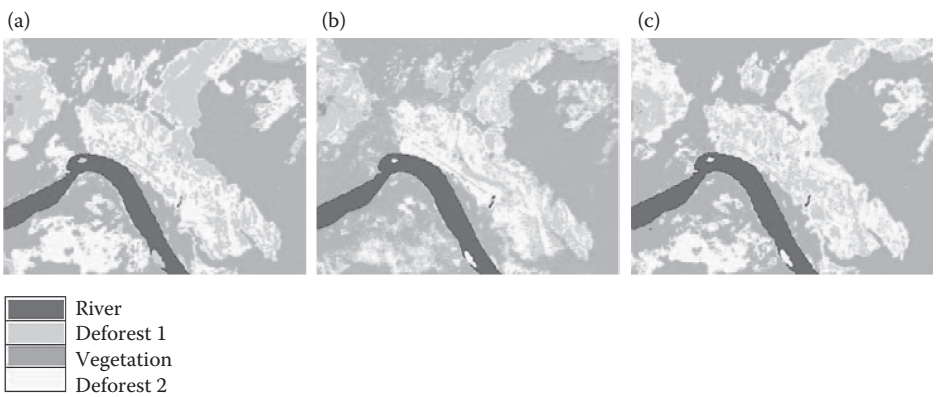

FIGURE 24.10 (**See color insert.**) Four-class ISODATA classification applied to (a) original MS image, (b) uHT SAR-MS fused image, and (c) GIM fused image.

means of the spectral angle mapper (SAM) shows that the Hermite transform method preserves the original spectral content with only a slightly larger spectral distortion in comparison with the GIM method. Moreover, an ISODATA classification experiment applied on the fused products confirms that the HT fusion method has the ability to better identify and separate classes in high-resolution image structures that were incorporated from the SAR image.

ACKNOWLEDGMENTS

This work was sponsored by UNAM PAPIIT grants IN113611 and IX100610, and the Centro de Investigación en Geografía y Geomática "Ing. Jorge L. Tamayo."

REFERENCES

1. C. Pohl and J. L. Van Genderen, Multisensor image fusion in remote sensing: Concepts, methods and applications, *International Journal of Remote Sensing*, 19(5), 823–854, 1998.
2. L. Wald, *Data Fusion Definitions and Architectures*, École des Mines de Paris, Paris, 2002.
3. G. Piella, A general framework for multiresolution image fusion from pixels to regions, *Information Fusion*, 4, 259–280, 2003.
4. W. J. Carper, T. M. Lillesand and R. W. Kiefer, The use of intensity-hue-saturation transform for merging SPOT panchromatic and multi-spectral image data, *Photogrammetric Engineering and Remote Sensing*, 56(4), 459–467, 1990.
5. P. S. Chavez and J. A. Bowell, Comparison of the spectral information content of Landsat thematic mapper and SPOT for three different sites in the Phoenix, Arizona region, *Photogrammetric Engineering and Remote Sensing*, 54(12), 1699–1708, 1988.
6. P. S. Chavez and A. Y. Kwarteng, Extracting spectral contrast in Landsat thematic mapper image data using selective principal component analysis, *Photogrammetric Engineering and Remote Sensing*, 55(3), 339–348, 1989.
7. Z. Wang, D. Ziou, C. Armenakis, D. Li and Q. Li. A comparative analysis of image fusion methods, *IEEE Transactions on Geoscience and Remote Sensing*, 43(6), 1391–1402, 2005.
8. D. A. Yocky, Image merging and data fusion by means of the two dimensional wavelet transform, *Journal of the Optical Society of America A*, 12(9), 1834–1841, 1995.
9. J. Zhou, D. L. Civco and J. A. Silander, A wavelet transform method to merge Landsat TM and SPOT panchromatic data, *International Journal of Remote Sensing*, 19, 743–757, 1998.
10. T. Ranchin and L. Wald, Fusion of high spatial and spectral resolution images: The ARSIS concept and its implementation, *Photogrammetric Engineering and Remote Sensing*, 66, 49–61, 2000.
11. B. Aiazzi, L. Alparone, S. Baronti and A. Garzelli, Context-driven fusion of high spatial and spectral resolution images based on oversampled multi-resolution analysis, *IEEE Transactions on Geoscience and Remote Sensing*, 40(10), 2300–2312, 2002.
12. J. Núñez, X. Otazu, O. Fors, A. Prades and R. Arbiol, Multiresolution-based image fusion with additive wavelet decomposition, *IEEE Transactions on Geoscience and Remote Sensing*, 37(3), 1204–1211, 1999.
13. S. G. Mallat, A theory for multiresolution signal decomposition: The wavelets representation, *Transactions* on *Pattern Analysis and Machine Intelligence*, 11(7), 674–693, 1989.
14. M. Holschneider, R. Kronland-Martinet, J. Morlet and P. Tchamitchian, A real-time algorithm for signal analysis with the help of wavelet transform, in *Wavelets, Time-Frequency Methods and Phase Space*. Springer-Verlag, Berlin, Germany, pp. 289–297, 1989.
15. M. J. Shensa, The discrete wavelet transform: Wedding the à trous and Mallat algorithm, *IEEE Transactions on Signal Processing*, 40, 2464–2482, 1992.
16. M. González-Audícana, J. L. Saleta, R. García Catalán and R. García, Fusion of multispectral and panchromatic images using improved IHS and PCA mergers base don Wavelet decomposition, *IEEE Transactions on Geoscience and Remote Sensing*, 42(6), 1291–1299, 2004.
17. M. González-Audícana, X. Otazu, O. Fors and J. A. Alvarez-Mozos, A low computational-cost method to fuse IKONOS images using the spectral response fuction of its sensors, *IEEE Transactions on Geoscience and Remote Sensing*, 44(6), 1683–1691, 2006.
18. F. Nencini, A. Garzelli, S. Baronti and Luciano Alparone, Remote sensing image fusion using the curvelet transform, *Information Fusion*, 8, 143–156, 2007.

Q8

19. J. B. Martens, Local orientation analysis in images by means of the Hermite transform, *IEEE Transactions on Image Processing*, 6(8), 1103–1116, 1997.
20. A. M. Van Dijk and J. B. Martens, Image representation and compression with steered Hermite transform, *Signal Processing*, 56, 1–16, 1997.
21. Alparone L., Baronti S., Garzelli A. and Nencini F., Landsat ETM+ and SAR image fusion based on generalized intensity modulation, *IEEE Transactions on Geoscience and Remote Sensing*, 42(12), 2832–2839, 2004.
22. H. Fang and S. Liang, Retrieving leaf area index with a neural network method: Simulation and validation, *IEEE Transactions Geoscience and Remote Sensing*, 41(9), 2052–2062, 2003.
23. A. Witkin, Scale-space filtering: A new approach to multiscale description, *Image Understand*, 3, 79–95, 1984.
24. T. Lindeberg, *Scale-Scale Theory in Computer Vision*, Kluwer Academic, Boston, MA, 1994. **Q9**
25. J. J. Koenderink and A. J. Van Doorn, Receptive field families, *Biological Cybernetics*, 63, 291–297, 1990.
26. S. Marcelja, Mathematical description of the responses of simple cortical cells, *Journal of the Optical Society of America.*, 70, 1297–1300, 1980.
27. J. G. Daugman, Two-dimensional spectral analysis of cortical receptive fields profiles, *Vision Research*, 20, 847–856, 1980.
28. M. Bastiaans, Gabor's signal expansion and degrees of freedom of a signal, *Optica Acta*, 29, 1223–1229, 1982.
29. M. Porat and M. Zeevi, The generalized gabor scheme of image representation in biological and machine vision, *IEEE Transactions* on *Pattern Analysis and Machine Intelligence*, 10(4), 454–467, 1988.
30. D. G. Stork and H. R. Wilson, Do Gabor functions provide appropriate descriptions of visual cortical receptive fields?, *Journal of the Optical Society of America A*, 7(8), 1362–1373, 1990.
31. R. A. Young, The Gaussian derivative theory of spatial vision: Analysis of cortical cell receptive field line-weighting profiles, Technical Report GMR-4920, General Motors Research Laboratories, Computer Science Department, Warren MI 48090, 1985.
32. R. A. Young, R. M. Lesperance and W. W. Meyer, The Gaussian model for spatial-temporal vision: I. Cortical model, *Spatial Vision*, 14(3,4), 261–319, 2001.
33. R. A. Young, "Oh say, can you see?," The physiology of vision, in *Human Vision, Visual Processing, and Digital Display II*, 1453 in *Proc. SPIE*, 92–123, 1991.
34. A. C. den Brinker and J. A. J. Roufs, Evidence for a generalized Laguerre transform of temporal events by the visual system, *Biological Cybernetics*, 67(5), 395–402, 1992.
35. Y. Jian and A. Reeves, Visual pattern encoding with weighted Hermite polynomials *Spatial Vision*, 14(3–4), 391–412, 2004.
36. Y. Jian and A. Reeves, Bottom-up visual image processing probed with weighted Hermite polynomials, *Neural Networks*, 8(5), 669–691, 1995.
37. L. M. J. Florack, B. M. ter Haar Romeny, J. J. Koenderink and M. A. Viergever, Scale and the differential structure of images, *Image and Vision Computing*, 10(6), 376–388, 1992.
38. J. J. Koenderink and A. J. V. Doorn, Representation of local geometry in the visual system, *Biological Cybernetics*, 55, 367–375, 1987.
39. J. J. Koenderink and A. J. V. Doorn, Generic neighborhood operators, *IEEE Transactions* on *Pattern Analysis and Machine Intelligence*, 14(6), 597–605, 1992.
40. J. B. Martens, The hermite transform—Theory, *IEEE Transactions on Acoustics, Speech and Signal Processing*, 38(9), 1607–1618, 1990.
41. J. B. Martens, The Hermite transform—Applications, *IEEE Transactions on Acoustics, Speech and Signal Processing*, 38(9), 1595–1606, 1990.
42. J. L. Silván-Cárdenas and B. Escalante-Ramírez, The multiscale Hermite transform for local orientation analysis, *IEEE Transactions on Image Processing*, 15(5), 1236–1253, 2006.
43. B. Escalante-Ramírez and J. L. Silván-Cárdenas, Advanced modeling of visual information processing: A multirresolution directional-oriented image transform based on Gaussian derivatives, *Signal Process*: *Image Communication*, 20(9–10), 801–812, 2005.
44. G. Szegö, *Orthogonal Polynomials*, American Mathematical Society, Colloquium Publications, 1959.
45. W. T. Freeman and E. H. Adelson, The design and use of steerable filters, *IEEE Transactions on Pattern Analysis and Machine Intelligence*, 13(9), 891–906, 1991.
46. B. Escalante-Ramírez and A. López-Caloca, Image fusion with the Hermite transform, in *Conf. ICIP 2003, International Conference on Image Processing* 14th, Barcelona, Spain.

47. B. Escalante-Ramírez and A. López-Caloca, The Hermite transform: An efficient tool for noise reduction and image fusion in remote-sensing, in *Signal and Image Processing for Remote Sensing*, C. H. Chen (ed.), Taylor & Francis, Boca Raton, FL, 2006.
48. M. Hashimoto and J. Sklansky, Multiple-order derivatives for detecting local image characteristics, *Computer Vision Graphics and Image Processing*, 39, 28–55, 1987.
49. H. Li, B. S. Manjunath and S. K. Mitra, Multisensor image fusion using the wavelet transform, *Graphical Models and Image Processing*, 57(3), 235–245, 1995.
50. D. L. Donoho, Denoising by soft-thresholding, *IEEE Transactions on Information Theory*, 41, 613–627, May 1995.
51. D. L. Donoho and I. M. Johnstone, Ideal spatial adaptation via wavelet shrinkage, *Biometrika*, 81, 425–455, 1994.
52. D. L. Donoho, Denoising by soft-thresholding, *IEEE Transactions on Information Theory*, 41, 613–627, 1995.
53. S. G. Chang, B. Yu and M. Vetterli, Spatially adaptive wavelet thresholding with context modeling for image denoising, *IEEE Transactions on Image Processing*, 9(9), 2000.
54. F. Argenti and L. Alparone, Speckle removal from SAR images in the undecimated wavelet domain, *IEEE Transactions on Geoscience and Remote Sensing*, 40(11), 2363–2373, 2002.
55. B. Escalante-Ramírez and J. Lira-Chávez, Performance-oriented analysis and evaluation of modern adaptive speckle reduction techniques in SAR images, *Visual Information Processing V*. SPIE-2753, 1996.
56. B. Escalante-Ramírez and J. B. Martens, Noise reduction in computerized tomography images by means of polynomial transforms, *Journal of Visual Communication and Image Representation*, 3(3), 272–285, 1992.
57. J. C. Price, Estimating leaf area index from satellite data, *IEEE Transactions on Geoscience and Remote Sensing*, 31(3), 727–734, 1993.
58. F. Baret, S. Jacquemoud and J. F. Hanocq, The soil concept in remote sensing, *Remote Sensing*, 7, 65–82, 1993.
59. M. González-Audícana, X. Otazu, O. Fors and A. Seco, Comparison between Mallat's and the 'à trous' discrete wavelet transform based algorithms for the fusion of multispectral and panchromatic images, *International Journal of Remote Sensing*, 26(3), 595–614, 2005.

Cat: #K12625 **Chapter 024**

TO: CORRESPONDING AUTHOR
AUTHOR QUERIES - TO BE ANSWERED BY THE AUTHOR

The following queries have arisen during the typesetting of your manuscript. Please answer these queries by marking the required corrections at the appropriate point in the text.

Q1	Is the change "we find the Gabor transform useful" OK?	
Q2	Please check if "0,. . .. . ..;∞, " is OK here.	
Q3	Please check if $l = 0, k$ is OK.	
Q4	Please describe the figure labels for Figure caption 24.2.	
Q5	Please check "Figure 24.1b . . . . . .respectively" is OK here.	
Q6	Is this nonlinear?	
Q7	The sentence beginning with "N=2" is incomplete. Please clarify.	
Q8	Please provide the editor's name in reference [14].	
Q9	Please confirm if it is T. Lindeberg as changed in reference [24].	
Q10	Please provide the page number in reference [53].	
Q11	Please cite reference [59] in the text.	